Engineering and detection of light scattering directionalities in dewetted nanoresonators through dark-field scanning microscopy

NICOLETTA GRANCHI,[1,9,*] LUCA FAGIANI,[2,3,9] MARCO SALVALAGLIO,[4,5] CHIARA BARRI,[2,3] ANDREA RISTORI,[1] MICHELE MONTANARI,[1] MASSIMO GURIOLI,[1] MARCO ABBARCHI,[6,7] AXEL VOIGT,[4,5] MARIA ANTONIETTA VINCENTI,[8] FRANCESCA INTONTI,[1] AND MONICA BOLLANI[2]

[1]*Department of Physics and Astronomy and LENS, University of Florence, Sesto Fiorentino, Italy*
[2]*Department of Physics, Politecnico di Milano, Milan, Italy*
[3]*Institute of Photonic and Nanotechnology - Consiglio Nazionale delle Ricerche, LNESS Laboratory, Como, Italy*
[4]*Institute of Scientific Computing, TU Dresden, 01062 Dresden, Germany*
[5]*Dresden Center for Computational Materials Science (DCMS), TU Dresden, 01062 Dresden, Germany*
[6]*Aix Marseille Univ, Université de Toulon, CNRS, IM2NP 13397, Marseille, France*
[7]*Solnil, 95 Rue de la République, 13002 Marseille, France*
[8]*Department of Information Engineering, University of Brescia, Brescia, Italy*
[9]*Equal contibutors.*
[*]*granchi@lens.unifi.it*

Abstract: Dewetted, SiGe nanoparticles have been successfully exploited for light management in the visible and near-infrared, although their scattering properties have been so far only qualitatively studied. Here, we demonstrate that the Mie resonances sustained by a SiGe-based nanoantenna under tilted illumination, can generate radiation patterns in different directions. We introduce a novel dark-field microscopy setup that exploits the movement of the nanoantenna under the objective lens to spectrally isolate Mie resonances contribution to the total scattering cross-section during the same measurement. The knowledge of islands' aspect ratio is then benchmarked by 3D, anisotropic phase-field simulations and contributes to a correct interpretation of the experimental data.

1. Introduction

All-dielectric Mie resonators have been widely studied and proposed as a valid alternative to plasmonic nanoparticles to improve light-matter interaction at the nanoscale [1,2]. Sub-wavelength optical resonators enable efficient manipulation of electromagnetic fields and can be used as building blocks for metamaterials and metasurfaces [3–8]. It has been demonstrated, both theoretically and experimentally, that monocrystalline all-dielectric islands support Mie resonances that can be tuned by properly scaling the geometrical dimensions of the resonator [2,9,10], opening new paths for optoelectronic applications [6,7,11]. All-dielectric nanoparticles can support multiple resonances from electric and magnetic modes of different order, which in turn allows the observation of different types of generalized Kerker effects [12–15]. This unidirectional scattering behavior, which is similar to classical antennas, results from constructive and destructive interference between electric and magnetic modes within the volume of the nanoparticles. High scattering directivity in combination with a high degree of flexibility for light direction is desirable for the effective operation of many practical optical devices, like

for example perfect mirrors or nanoheating devices [16–18], and systems that can be used for optical nanocircuitry and sensing. For this purpose, several designs, such as V-shaped antenna and asymmetric dimer configuration, have been recently proposed [19–21]. Also in plasmonics, light scattering directionality has already been exploited to improve spectroscopic performances [22,23].

Here we demonstrate that, when light is tilted with respect to the axis normal to the nanoislands, different modes sustained by a SiGe-based nanoantenna with a simple and symmetric shape translate into radiation scattered in different directions. We developed an approach that is complementary to more conventional, back focal plane spectroscopy [15,24–26] that usually aims at imaging the Fourier space through a selection of wavevectors k. In our work, we exploit the scanning of the sample below the collection objective lens of a dark-field microscope under tilted illumination to obtain a different type of data. The collection objective lens collects a spectrum in every position of the sample. The hyperspectral set of data allows us, in one measurement, to spectrally isolate the different contributions of each Mie resonance to the total scattering cross section in a single SiGe island. So far, this result has been achieved by changing the polarization of the illumination source and hence by performing two separate measurements [27–29]. Notably, our method reveals that important information could be lost in conventional/custom-built dark-field setups operating with tilted illumination when the scattering cross sections of a scatterer is assessed through the acquisition of a single spectrum.

The dielectric monocrystalline, atomically smooth nanoantennas analyzed in this work are realized via solid- state dewetting, by exploiting the natural instability of thin films to form a variety of nanostructures with high fidelity over hundreds of repetitions and extremely large scales [8,30–33]. This method has emerged among several alternatives as one of the most convenient approaches thanks to its scalability [30,34] and the possibility to form ordered [31,35] and disordered structures [32] via self-assembly. In order to compare the experimental data with theoretical predictions, we performed 3D phase-field simulations that account for the correct equilibrium shape of the SiGe dewetted islands and thus for the islands' vertical aspect ratio (*AR*), that strongly affects the spectral positions of the detected resonances.

2. Methods and materials

2.1. Fabrication

Our samples consist of arrays of $Si_{0.7}Ge_{0.3}$ nanoislands obtained through a hybrid top-down/bottom-up approach based on the natural morphological evolution of thin solid films. The initial thickness of the top $Si_{0.7}Ge_{0.3}$ film is 26 nm, deposited over a monocrystalline, (001)-oriented, silicon- on insulator (SOI) wafer with a device thickness of 7 nm and a buried SiO_2 layer of 25 nm. Squared $Si_{0.7}Ge_{0.3}$ patches with initial aspect ratio $AR_0 = h(t)/R(t)|_{t=0}$ (with $h(0)$ the film thickness and R half of the patch dimension along the [110] direction) are fabricated by means of electron beam lithography (EBL) and reactive ion etching (RIE); upon annealing, they undergo a solid-state dewetting process forming self-assembled monocrystalline faceted islands [35,36]. Details on the fabrication process can be found in Supplement 1 (section S1a). The SEM images, reported in Figs. 1(a)–(c), show different realizations of the same SiGe system. Experimentally, a final average aspect ratio *AR* = 0.6 is measured. The islands exhibit a clear faceting, including in particular {001}, {113} and {111} facets with junctions and connections to the substrate that may be ascribed to higher index facets (Fig. 1(a)–(c)), compatible with the highest aspect-ratio shapes observed in SiGe islands with respect to pure Si-islands [37,38].

2.2. Simulations

The theoretical assessment of the dewetting process, identifying the main driving forces at play and reporting on the expected morphologies, is carried out through three-dimensional
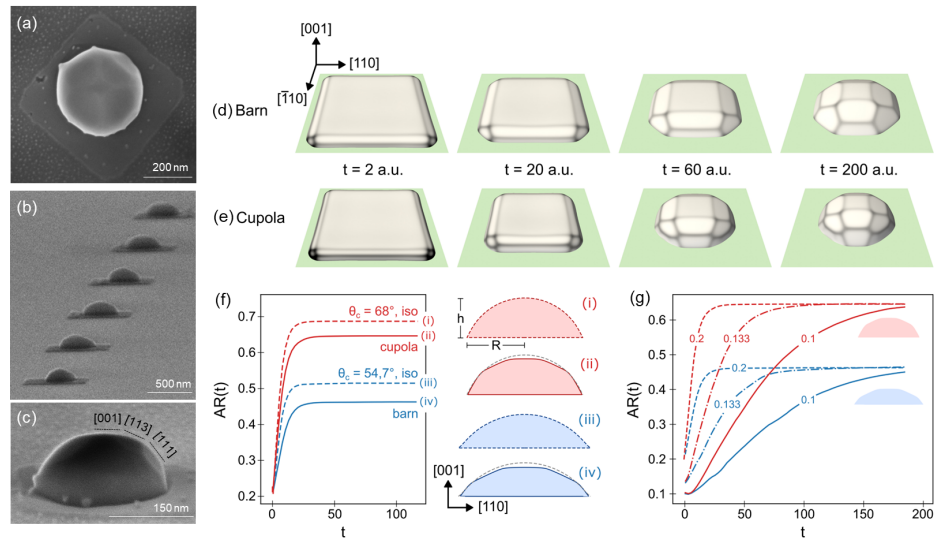
Fig. 1. **(a)** SEM top view image of a single dewetted $Si_{0.7}Ge_{0.3}$ island. **(b)** SEM image of islands acquired with a tilt angle of 45 degrees with respect the sample normal to highlight the faceting of each scatterer. **(c)** SEM image of of a single island, where the faceting planes {001}, {113} and {111} are labelled. **(d)-(e)** Phase field simulation of solid-state dewetting of patches (initial aspect ratio AR_0=0.2) with morphologies and contact angle compatible with a barn and cupola shapes [36], respectively. **(f)** Comparison of aspect ratio over time [$AR(t)$] for the evolution in panel (d) and (e), together with the same quantity for phase field (PF) simulations with isotropic surface energy (left) and corresponding equilibrium shapes with dashed lines corresponding to the isotropic case (right). **(g)** $AR(t)$ in the range $AR_0 \in [0.1; 0.2]$ for both barn (blue) and cupola (red) morphologies.

phase-field (PF) model of surface diffusion [39–41] which proved powerful in reproducing solid-state dewetting in 3D [31,32,35,42].

We provide a theoretical assessment of the process, crucial to determine the features of Mie scattering. The surface of the solid phase is described implicitly as a diffused interface among two phases (solid-vacuum). Crystal faceting is accounted for through a suitable parameterization of the surface energy density reproducing energetics of $Si_{0.7}Ge_{0.3}$ surfaces and a regularization of sharp corners [43,44]. An average contact angle with the substrate is imposed through a Neumann boundary condition [42,45]. Details are reported in Supplement 1 (S1b).

Light scattering simulations are performed by means of Finite Element Method (FEM) and Finite Difference Time Domain (FDTD) commercial softwares, respectively Comsol Multiphysics [46] and Lumerical [47]. FEM simulations are used in order to explore how the Mie resonances can be tuned by changing AR within the accessible range, while FDTD simulations are exploited to reproduce the experimental conditions through the use of a broadband tilted illumination source (Supplement 1, S3).

2.3. Experimental setup

In order to perform the Dark-field Scanning Optical Microscopy (SDOM) experiment we employ a custom-built setup in which the dark-field condition is achieved by illuminating the islands with a light source tilted by an angle of 30°, larger than the collection angle of the objective lens (NA = 0.45), with respect to the axis normal to the substrate. The illumination source is a supercontinuum laser and the illumination spot has a diameter of approximately 20 μm. The

objective lens collects the scattered light, that is then fed into a multimode optical fiber of 10 μm diameter before being dispersed by a monochromator and detected with a Si-based CCD camera. For more details on the experimental setup see Supplement 1 (S1d). The presence of the 10 μm core optical fiber in the collection branch acts as a spatial filter, and the corresponding collection spot has a diameter of ≈ 1 μm. The sample is mounted on a xy piezoelectric stage that allows to obtain dark-field spatially-resolved maps, collecting a single scattering spectrum for every position of the nanoantenna.

3. Results and discussion

We begin with the theoretical assessment of the islands' morphologies obtained by the (solid-state) dewetting process, and discuss the dependence of Mie resonances on the resulting geometrical features. According to the faceting observed in experiments (Fig. 1(a)–(c)), we focus, for the sake of thoroughness, on both morphologies exhibiting {001}, {113} and {111} facets in SiGe systems, i.e. the shapes called *barn* and *cupola* [37], with average contact angles of ∼ 54,7° and ∼ 68°, respectively. The cupola morphology features additional facets such as {322} and {715} and {12 3 5}, here described through an averaging of facets with similar slopes (see Supplement 1, S1b). The morphological evolution for the considered shapes, owing to their relatively large AR, proceeds with nucleation and widening of facets from the sides of the initial patch [35] [Fig. 1(d)–(e)]. Therefore, the process allows for smooth changes of morphological features by tuning the annealing time and/or annealing temperature. A final aspect ratio, AR_∞ 0.46 and 0.65 is achieved for the barn-like and the cupola-like islands, respectively [Fig. 1(f)]. The latter matches well the experimental results, suggesting a cupola-like morphology for the dewetted islands [see Fig. 1(c)].

Notice that a shallower shape for the barn with respect to the cupola is expected owing to the smaller contact angle. In addition, however, the actual AR depends on the faceting, as can be devised by Fig. 1(f) comparing the results obtained with and without surface energy anisotropy but same contact angles. We find that a logistic equation $AR(t) = [2(1 + e^{-t/\tau})^{-1} - 1](AR_\infty - AR_0) + AR_0$ with τ a characteristic time considered here as a fitting parameter, well approximates the evolution of the AR [Fig. 1(f)], and can be used to calibrate the dewetting process when targeting a specific shape. This approximation is expected to be less accurate when decreasing AR_0 owing to the onset of other instabilities, such as rims formation and depletion of material from the center of the patch, i.e., deviation from the increase of aspect ratio of a convex island shape as in Fig. 1(d)-(e) [35].

Still, in a range of AR_0 within 0.1-0.2, similar qualitative evolutions are observed, with different scaling of the AR in time [Fig. 1(g)]. We can conclude that the dewetted particles having an aspect ratio of ∼0.6 in the experiments should exhibit a morphology compatible with a cupola-like faceted shape. Also, such an aspect ratio is very close to the equilibrium one, thus pointing to highly stable structures with reproducible morphologies obtained via the considered self-assembly process.

To explore how the Mie resonances can be tuned by changing AR within the accessible range, we perform FEM simulations of light scattering. Figure 2(a) shows a schematic representation of a SiGe nanoantenna above a 7 nm thick Si pedestal (visible also in the SEM images of Fig. 1(a), (b) and (c) and a SiO_2 box of 25 nm separating it from the Si-bulk. As shown in the upper right inset of Fig. 2(a), the nanoantenna is modelled with faceting angles corresponding to the crystallographic planes observed in the experiments and considered for the phase-field morphologies. The FEM scattering cross-section of a faceted resonator of radius $R = 200$ nm is reported in Fig. 2(b) for different values of AR (from 0.3 to 0.7). Details of FEM simulations are reported in Supplement 1 (S1c). In the map of Fig. 2(b), starting from the maximum value of AR = 0,7, two broad resonances are distinguishable ($\lambda \approx 600$ nm and $\lambda \approx 750$ nm).
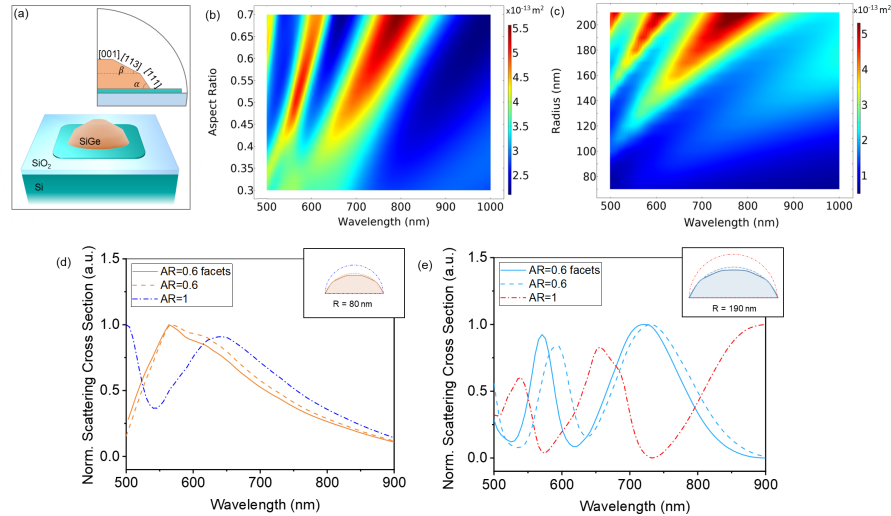
Fig. 2. (a) Sketch of the model used in FEM simulations: a SiGe resonator above a 7 nm thick Si pedestal and a SiO$_2$ box of 25 nm separating it from the Si-bulk. In the top right inset, the crystallographic planes are labelled, together with the faceting angles $\alpha = 54.7°$ and $\beta = 25.2°$. **(b)** FEM Scattering cross-section for an island of $R = 200$ nm as a function of *AR* (vertical axis) and wavelength (horizontal axis). **(c)** FEM Scattering cross-section of an island as a function of R and wavelength for $AR = 0.6$. **(d)** Normalized scattering cross sections, respectively of an island of radius $R = 80$ nm obtained when modeling the nanoantenna with *AR*=0.6 and the faceting (orange solid line), with a cut hemisphere of *AR*=0.6 (orange dashed line) and with a hemisssssphere of *AR*=1 (dark blue dashed-dot line). **(e)** Scattering cross sections, respectively of an island of radius $R = 190$ nm obtained when modeling the nanoantenna with *AR*=0.6 and the faceting (blue solid line), with a cut hemisphere of *AR*=0.6 (blue dashed line) and with an hemisphere of *AR*=1.0 (red dashed-dot line).

The identification of Mie modes is performed by studying the field profiles inside the nanoparticle and identifying the corresponding current loops [11,48]; the resonance centered around $\lambda \approx 750$ nm can be attributed to electric (ED) and magnetic dipole (MD), that are not distinguishable owing to effects of symmetry breaking with respect to the ideal case of a spherical Mie resonator in air. We label this band ED/MD [48,49]. We attribute the band spectrally centered around 600 nm mainly to a magnetic quadrupole (MQ) contribution, while, decreasing *AR*, we observe a blue-shift of the resonances. Differently from the *AR*, the radius R is directly related to the initial size of the EBL patterned SiGe area, R_0.

In order to assess the influence of the radius in this peculiar morphology of the island, we simulated the scattering of nano-islands by tuning this parameter from $R = 70$ nm to $R = 210$ nm [Fig. 2(c)] for $AR = 0.6$, as from experiments and PF simulations for cupola morphologies of dewetted islands. Resonant modes can be identified as in Fig. 2(b): a red-shift is observed for increasing values of R, whereas for a value of roughly $R = 100$ nm the scattering resonances become weaker.

These simulations are used as a tool for comparison with experimental data for which the correct *AR* assessed by PF simulations is crucial; to confirm the accuracy of our approach, we show how the Mie resonances are affected by different approximations, namely neglecting contributions of surface-energy anisotropy and contact angle. Specifically, we report in Fig. 2(d) and (e) the scattering cross sections of an island of radius $R = 80$ nm and 190 nm, respectively, obtained

with three different models: nanoantenna with faceting and *AR*=0.6 (solid line), nanoantenna as a cut hemisphere with *AR* = 0.6, and finally, as a hemisphere with *AR*=1.0. Figure 2(d)–(e) indicates, for both values of R, how the *AR* is decisive in changing the entire scattering cross section. We note that considering a hemisphere with the equilibrium aspect-ratio obtained from PF simulations represents a rather good shape approximation, at least for smaller nanoantennas, even though differences can be seen in Fig. 2 and may be relevant for fine tuning.

We now introduce the role of the tilted illumination through FDTD simulations. Recently, in [49] it was shown how the near-field distribution of nanoantennas is affected by the angle of illumination. Here, we extend it to the far-field, and show in Fig. 3 how the far-field plots change by tilting the illumination source; in particular, we simulated the scattering of the faceted island of *R* = 190 nm and *AR* = 0.6 under the illumination of a plane wave at normal incidence and then tilted by 30° and 60° with respect to the normal to the substrate plane (Fig. 3(a)). We plot the angular scattering of the electric field intensity along the two axes of the k-space both for MQ [Fig. 3(b)] and ED/MD [Fig. 3(c)] for θ = 0°, 30°, 60°. We observe that for both Mie resonances the angular distribution is decentralized towards the left direction due to the lateral illumination from the plane-wave (coming from the right side), and this effect is more intense as the illumination angle is increased. This confirms that the beam steering properties of Mie resonators can be modulated, enhanced, or suppressed by playing with the illumination angle. We can thus infer that tilted illumination can be used as an efficient tool to modulate the beam steering properties of nano-antennas with a simple and symmetric shape. In other words, we can use tilted illumination to redirect and control light directionality.
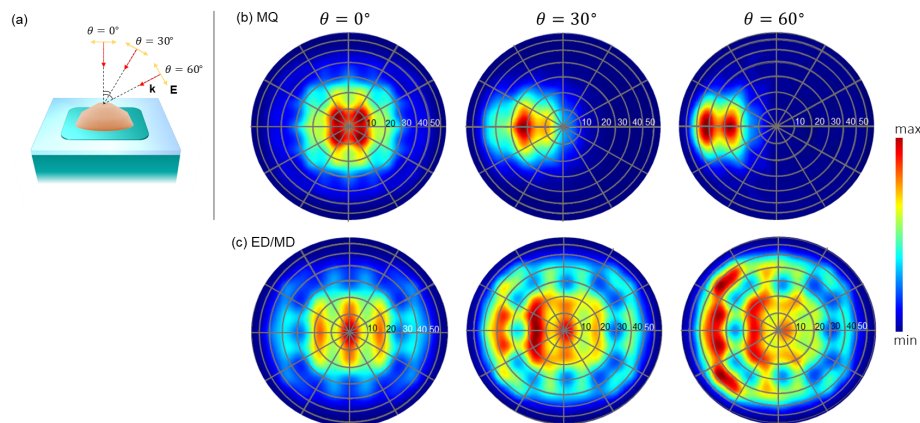

Fig. 3. (a) Sketch of the model used in FDTD simulations: the island is illuminated by an illumination source normal to the substrate plane, then tilted by an angle θ = 30° and θ = 60° with respect to the normal axis. **(b)** FDTD polar plots (or Fourier space maps) of mode MQ in the three cases of illumination angles. **(c)** FDTD polar plots (or Fourier space maps) of mode ED/MD in the three cases of illumination angles.

We performed a SDOM experiment [Fig. 4(a)] (details on the experimental setup can be found in Methods and Materials section). The reconstructed hyperspectral maps can be filtered around a single wavelength, or around a broad interval, like the one shown in the upper right inset of Fig. 4(b), obtained on an island of $R \approx 190$ nm [upper left inset of Fig. 4(b)] in the spectral range 500-900 nm.

This imaging method represents an innovative way of managing the information gathered from dark-field experiments: the overlapped spectra reported in Fig. 4(b) are obtained by performing a horizontal cut of 1.8 μm in the central region of the hyperspectral map (shown in the inset) and are reported in a color-scale that reproduces the direction of the cut, from pixel A (yellow)
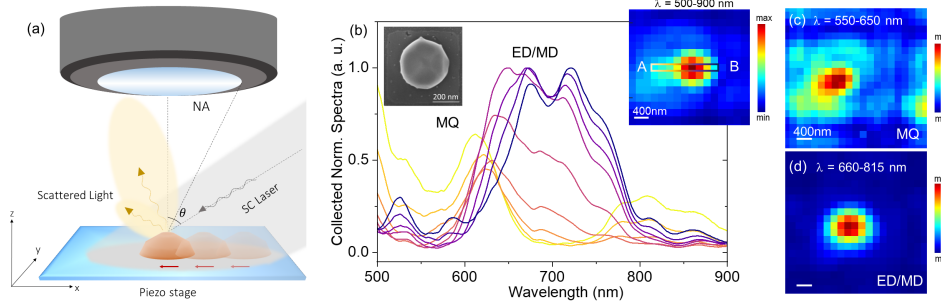
Fig. 4. (a) Sketch of the SDOM setup. **(b)** Dark-field spectra of the island $R = 190\,\text{nm}$ normalized to the Supercontinuum source. The upper left inset displays a SEM top view image of the investigated scatterer. The spectra are obtained by performing a horizontal cut on the hyperspectral map reported in the upper right inset, filtered around the entire wavelength interval (500-900 nm). The cut is highlighted with a colored rectangle, and the color scale of the spectra reproduces the direction of the cut, from pixel A (yellow) to pixel B (blue). **(c)-(d)** Dark-field maps filtered around a wavelength interval that correspond to MQ and ED/MD (respectively $\lambda \approx [550–650]$ nm and [660–815] nm).

to pixel B (blue). Each pixel of the cut corresponds to a single spectrum normalized to the illumination source spectrum, acquired in adjacent pixels of the map.

The two main Mie resonances MQ and ED/MD are labelled through the match of the spectra with the FEM scattering cross-section of an island of $R = 190\,\text{nm}$ and $AR = 0.6$. A modulation of the signal and significant variations of the relative weights of the peaks can be observed. Conventional dark-field measurements employing a tilted illumination and acquisition of a spectrum in a single position downstream of a collection fiber [2,9,10], limit the amount of information that can be inferred from the far-field scattering of nano-antennas, that determines a modulation in the scattered signal, showing a peculiar spatial dependence for each mode that should not be neglected. This information is here given by the different weights of the peaks in different spatial positions of the cut. We attribute the observed effect to a combination of the islands beam steering properties under the inclination of the illumination source and the collection configuration/geometry. From FDTD simulations we know that because of the illumination tilted by an angle 30°, each Mie mode hotspot points toward different angles, specifically $\approx 25°$ for MQ, $\approx 0°$ and 15° for ED/MD (see Fig. 3). For this reason, by spectrally filtering the dark-field hyperspectral map, in the right inset of Fig. 4(b) around the wavelength intervals corresponding to MQ and ED/MD, we find how the electric field maximum intensity scattered by the island exhibits different directions, i.e., the collected signal can change position for different wavelengths (see Supplementary Information S2). The Dark-field maps filtered around a wavelength interval that corresponds to MQ ($\lambda \approx [550–650]$ nm) and ED/MD, ($\lambda \approx [660–815]$ nm) are reported in Figs. 4(c) and 4(d), respectively. The two intervals were chosen to match the bandwidth of each peak in the corresponding scattering cross section obtained from FEM simulations. This can indeed be related to the different weights of the peaks observed in the spectra of Fig. 4(b): the spectra acquired along the horizontal direction (from left to right in the map) exhibit more intense peaks at lower wavelength in the left part of the cut (yellow), and the weights of the peaks increase for higher wavelengths as the right part of the cut is reached (blue). This effect is the result of a different directional light scattering that is selected by the collection system at different scan positions.

The features described above allow us to spectrally isolate the scattering contribution of the two main Mie resonances of a single nanoantenna, as described as follows. In Fig. 5 we show

a comparison between numerical simulations and experimental results on islands of different size. Dark-field spectra for islands of radius ≈ 80 nm and ≈ 190 nm are shown in Fig. 5(a) (upper panel, orange curve) and Fig. 5(b) (upper panel, blue curve), respectively, and the insets show the SEM images of the scatterers.
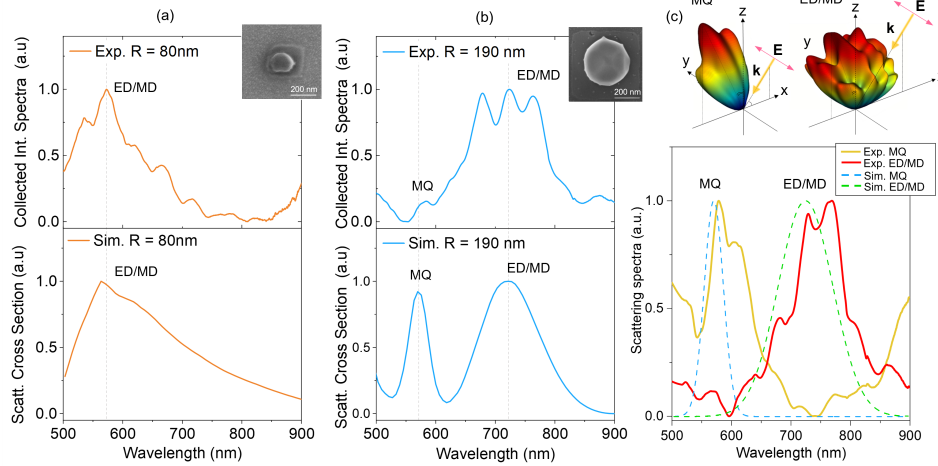

Fig. 5. (a) Upper panel: Dark-field signal obtained by integrating all the spectra acquired on an area of 10 px x 10 px (2 μm x 2 μm) from the hyperspectral map acquired by scanning a nanoantenna of $R \approx 80$ nm. Bottom panel: FEM scattering cross section of a faceted nanoantenna of $R = 80$ nm. **(b)** Upper panel: Dark-field signal obtained by integrating all the spectra acquired on an area of 10 px x 10 px (2 μm $\times$ 2 μm) from the hyperspectral map acquired by scanning a nanoantenna of $R \approx 190$ nm. Bottom panel: FEM scattering cross section of a faceted island of $R = 190$ nm. The insets show the SEM top view images of the two nanoantennas. **(c)** Upper panel: FDTD 3D radiation plots of MQ and ED/MD for $R = 190$ nm; in the graph are reported the spectral contributions, respectively in yellow and red, obtained by integrating the signal in the areas of maximum intensity of MQ and ED/MD (see S2 for details on the maps). The blue and green dashed lines are the theoretical contributions of MQ and ED/MD to the FEM total scattering cross-section.

The experimental scattering spectra derive from the correspondent dark-field hyperspectral maps, by integrating the spectra acquired on an area of 100 px^2 (4 μm^2); this integration step (see Supplement 1, S3) allows to compare the experimental data with the FEM scattering cross-sections of the two islands, reported in the bottom panels of Fig. 5(a) and (b). The theoretical curves were obtained with $AR = 0.6$ for both nanoantennas, and a radius of $R = 80$ nm and $R = 190$ nm respectively for the smaller and larger islands (orange and blue curve, respectively). Dark-field spectra fit quite well the theoretical peaks. As expected, the smaller island (bottom panel) exhibits only the ED/MD type resonance, while the larger one shows two main peaks, MQ ($\lambda \approx 570$ nm) and ED/MD ($\lambda \approx 650$ nm). Deviations between experimental and theoretical spectra can be attributed to the fact that FEM simulations are not considering imperfections and asymmetries in the actual nanoantennas shape. Moreover, while the calculated spectra are very smooth, fine structures appear in the measured scattering spectra; this effect is due to some irregularities present in the spectrum of the employed supercontinuum laser.

As highlighted in Fig. 3, MQ and ED/MD exhibit a different behavior in the far-field that is further enhanced by the tilted illumination. In our system, the spectral modulation collected in the hyperspectral data, can be exploited for the first time to spectrally isolate the scattering contribution of the Mie resonances. In fact, by integrating the signal of the dark-field hyperspectral

maps of Fig. 4(c)–(d) throughout the areas where MQ and ED/MD exhibit their maximum intensity, we obtain two spectra, respectively the yellow and red curve in Fig. 5(c), that nicely agree with the theoretical contributions to the total scattering cross-section of MQ and ED/MD (blue and green dashed lines). Note that both spectra derive from a single scan and were therefore acquired simultaneously. So far, such different spectral components have been isolated only theoretically [50,51], or experimentally with the need of illumination with different polarizations [27–29].

4.   Conclusions

In summary, we addressed the theoretical modelling and characterized in detail the optical properties of all-dielectric, dewetted, SiGe-based Mie resonators. We numerically demonstrate that, upon tilted illumination, a single island generates radiation patterns pointing in different directions, depending on the selected Mie resonance.

The experimental results of dark-field scanning microscopy are supported by accurate information on the vertical aspect ratio of the islands obtained by phase-field simulations and light-scattering simulations, assessing the impact of island morphologies on optical properties. Our technique, by combining a lateral illumination with the controlled movement of the scatterer, represents a significant advance with respect to conventional dark-field spectroscopy of light scatterers, since it allows to spectrally isolate the two main Mie resonances contribution to the total scattering cross-section simultaneously. The detection of how scattering directionalities can be tuned through tilted illumination is a fundamental achievement in sight of far-field experimental necessities, like coupling into optical fibers and light harvesting for quantum optics. Moreover, in our study, this tunable approach to influence the scattering directivity of nano-antennas is combined with scalable fabrication methods, representing a step toward the realization of metasurfaces for different optoelectronic applications.

Disclosures. The authors declare that there are no conflicts of interest related to this article.

Data Availability. Data underlying the results presented in this paper are not publicly available at this time but may be obtained from the authors upon reasonable request.

Supplemental document. See Supplement 1 for supporting content.

References

1. A. B. Evlyukhin, S. M. Novikov, U. Zywietz, R. L. Eriksen, C. Reinhardt, S. I. Bozhevolnyi, and B. N. Chichkov, "Demonstration of Magnetic Dipole Resonances of Dielectric Nanospheres in the Visible Region," Nano Lett. **12**(7), 3749–3755 (2012).
2. A. I. Kuznetsov, A. E. Miroshnichenko, M. L. Brongersma, Y. S. Kivshar, and B. Luk'yanchuk, "Optically resonant dielectric nanostructures," Science **354**(6314), 6314 (2016).
3. B. Rolly, B. Bebey, S. Bidault, B. Stout, and N. Bonod, "Promoting Magnetic Dipolar Transition in Trivalent Lanthanide Ions with Lossless Mie Resonances," Phys. Rev. B: Condens. Matter Mater. Phys. **85**(24), 245432 (2012).
4. M. K. Schmidt, R. Esteban, J. J. Sáenz, I. Suárez-Lacalle, S. Mackowski, and J. Aizpurua, "Dielectric Antennas; A Suitable Platform for Controlling Magnetic Dipolar Emission," Opt. Express **20**(13), 13636–13650 (2012).
5. L. Shi, T. U. Tuzer, R. Fenollosa, and F. Meseguer, "A New Dielectric Metamaterial Building Block with a Strong Magnetic Response in the Sub-1.5-Micrometer Region: Silicon Colloid Nanocavities," Adv. Mater. **24**(44), 5934–5938 (2012).
6. Y. Yang, I. I. Kravchenko, D. P. Briggs, and J. Valentine, "All-dielectric metasurface analogue of electromagnetically induced transparency," Nat. Commun. **5**(1), 5753–5757 (2014).
7. A. Cordaro, J. Van De Groep, S. Raza, E. F. Pecora, F. Priolo, and M. L. Brongersma, "Antireflection high-index metasurfaces combining mie and fabry-perot resonances," ACS Photonics **6**(2), 453–459 (2019).
8. T. Wood, M. Naffouti, J. Berthelot, T. David, J. B. Claude, L. Métayer, A. Delobbe, L. Favre, A. Ronda, I. Berbezier, N. Bonod, and M. Abbarchi, "All-dielectric color filters using SiGe-based Mie resonator arrays," ACS Photonics **4**(4), 873–883 (2017).

9. S. Checcucci, T. Bottein, J. Claude, T. Wood, M. Putero, L. Favre, M. Gurioli, M. Abbarchi, and D. Grosso, "Titania-Based Spherical Mie Resonators Elaborated by High-Throughput Aerosol Spray: Single Object Investigation," Adv. Funct. Mater. **28**(31), 1801958 (2018).

10. D. Toliopoulos, M. Khoury, M. Bouabdellaoui, N. Granchi, J. B. Claude, A. Benali, I. Berbezier, D. Hannani, A. Ronda, J. Wenger, M. Bollani, M. Gurioli, S. Sanguinetti, F. Intonti, and M. Abbarchi, "Fabrication of spectrally sharp Si-based dielectric resonators: combining etaloning with Mie resonances," Opt. Express **28**(25), 37734–37742 (2020).

11. J. Van de Groep and A. Polman, "Designing dielectric resonators on substrates: Combining magnetic and electric resonances," Opt. Express **21**(22), 26285–26302 (2013).

12. M. Kerker, D. S. Wang, and C. Giles, "Electromagnetic scattering by magnetic spheres," J. Opt. Soc. Am. **73**(6), 765–767 (1983).

13. S. Kruk and Y. Kivshar, "Functional meta-optics and nanophotonics governed by Mie resonances," ACS Photonics **4**(11), 2638–2649 (2017).

14. W. Liu and Y. Kivshar, "Generalized Kerker effects in nanophotonics and meta-optics," Opt. Express **26**(10), 13085 (2018).

15. M. Khoury, H. Quard, T. Herzig, J. Meijer, S. Pezzagna, S. Cueff, M. Abbarchi, H. S. Nguyen, N. Chauvin, and T. Wood, "Light Emitting Si-Based Mie Resonators: Toward a Huygens Source of Quantum Emitters," Adv. Opt. Mater. **10**(21), 2201295 (2022).

16. Y. Yu, Y. Li, R. Salas-Montiel, and D. Qiao, "Perfect magnetic mirror based on magnetic dipole scattering in all-dielectric resonators," J. Appl. Phys. **131**(15), 153101 (2022).

17. Y. Li, X. Yang, Y. Yang, B. Wang, X. Li, and R. Salas-Montiel, "Optical nanoheating of resonant silicon nanoparticles," Opt. Express **27**(21), 30971–30978 (2019).

18. A. K. González-Alcalde, M. A. G. Mandujano, R. Salas-Montiel, L. O. Le Cunff, G. Lerondel, and E. R. Méndez, "Magnetic mirror metasurface based on the in-phase excitation of magnetic dipole and electric quadrupole resonances," J. Appl. Phys. **125**(24), 243103 (2019).

19. J. Q. Li, N. Verellen, D. Vercruysse, T. Bearda, L. Lagae, and P. V. Dorpe, "All-Dielectric Antenna Wavelength Router with Bidirectional Scattering of Visible Light," Nano Lett. **16**(7), 4396–4403 (2016).

20. T. Shibanuma, T. Matsui, T. Roschuk, J. Wojcik, P. Mascher, P. Albella, and S. A. Maier, "Experimental Demonstration of Tunable Directional Scattering of Visible Light from All-Dielectric Asymmetric Dimers," ACS Photonics **4**(3), 489–494 (2017).

21. Y. Yu, J. Liu, Y. Yu, D. Qiao, Y. Li, and R. Salas-Montiel, "Broadband unidirectional transverse light scattering in a V-shaped silicon nanoantenna," Opt. Express **30**(5), 7918–7927 (2022).

22. J. J. Mock, R. T. Hill, A. Degiron, S. Zauscher, A. Chilkoti, and D. R. Smith, "Distance-Dependent Plasmon Resonant Coupling between a Gold Nanoparticle and Gold Film," Nano Lett. **8**(8), 2245–2252 (2008).

23. G. C. Li, Q. Zhang, S. A. Maier, and D. Lei, "Plasmonic particle-on-film nanocavities: a versatile platform for plasmon-enhanced spectroscopy and photochemistry," Nanophotonics **7**(12), 1865–1889 (2018).

24. D. Y. Vercruysse, N. Sonnefraud F, B. Verellen, G. Fuchs, L. Di Martino, V. V. Lagae, S. Moshchalkov, A. Maier, and P. V. Dorpe, "Unidirectional Side Scattering of Light by a Single-Element Nanoantenna," Nano Lett. **13**(8), 3843–3849 (2013).

25. T. Rothe, M. Schmitz, and A. Kienle, "Angular and spectrally resolved investigation of single particles by darkfield scattering microscopy," J. Biomed. Opt. **17**(11), 117006 (2012).

26. L. Chen, M. Lopez-Garcia, M. P. C. Taverne, X. Zheng, Y. L. D. Ho, and J. Rarity, "Direct wide-angle measurement of a photonic band structure in a three-dimensional photonic crystal using infrared Fourier imaging spectroscopy," Optica **42**(8), 1584–1587 (2017).

27. T. Hinamoto, M. Hamada, H. Sugimoto, and M. Fujii, "Angle-, Polarization-, and Wavelength-Resolved Light Scattering of Single Mie Resonators Using Fourier-Plane Spectroscopy," Adv. Opt. Mater. **9**(8), 2002192 (2021).

28. J. Xiang, J. Chen, S. Lan, and A. E. Miroshnichenko, "Nanoscale Optical Display and Sensing Based on the Modification of Fano Lineshape," Adv. Opt. Mater. **8**(16), 2000489 (2020).

29. T. Hinamoto, S. Hotta, H. Sugimoto, and M. Fujii, "Colloidal Solutions of Silicon Nanospheres toward All-Dielectric Optical Metafluids," Nano Lett. **20**(10), 7737–7743 (2020).

30. M. Abbarchi, M. Naffouti, B. Vial, A. Benkouider, L. Lermusiaux, L. Favre, A. Ronda, S. Bidault, I. Berbezier, and N. Bonod, "Wafer Scale Formation of Monocrystalline Silicon-Based Mie Resonators via Silicon-on-Insulator Dewetting," ACS Nano **8**(11), 11181–11190 (2014).

31. M. Bollani, M. Salvalaglio, A. Benali, M. Bouabdellaoui, M. Naffouti, M. Lodari, S. Di Corato, A. Fedorov, A. Voigt, I. Fraj, L. Favre, J. B. Claude, D. Grosso, G. Nicotra, A. Mio, A. Ronda, I. Berbezier, and M. Abbarchi, "Templated dewetting of single-crystal sub-millimeter-long nanowires and on-chip silicon circuits," Nat. Commun. **10**(1), 5632 (2019).

32. M. Salvalaglio, M. Bouabdellaoui, M. Bollani, A. Benali, L. Favre, J. B. Claude, J. Wenger, P. De Anna, F. Intonti, A. Voigt, and M. Abbarchi, "Hyperuniform Monocrystalline Structures by Spinodal Solid-State Dewetting," Phys. Rev. Lett. **125**(12), 126101 (2020).

33. L. Fagiani, N. Granchi, A. Zilli, C. Barri, F. Rusconi, M. Montanari, E. Mafakheri, M. Celebrano, M. Bouabdellaoui, M. Abbarchi, F. Intonti, A. Khursheed, P. Biagioni, M. Finazzi, M. A. Vincenti, and M. Bollani, "Linear and nonlinear optical properties of dewetted SiGe islands," Opt. Mater.: X **13**, 100116 (2022).

34. A. Benali, J. B. Claude, N. Granchi, S. Checcucci, M. Bouabdellaoui, M. Zazoui, M. Bollani, M. Salvalaglio, J. Wenger, L. Favre, D. Grosso, A. Ronda, I. Berbezier, M. Gurioli, and M. Abbarchi, "Flexible photonic devices based on dielectric antennas," J. Phys. Photonics **2**(1), 015002 (2020).

35. M. Naffouti, R. Backofen, M. Salvalaglio, T. Bottein, M. Lodari, A. Voigt, T. David, A. Benkouider, I. Fraj, L. Favre, A. Ronda, I. Berbezier, D. Grosso, M. Abbarchi, and M. Bollani, "Complex dewetting scenarios of ultrathin silicon films for large-scale nanoarchitectures," Sci. Adv. **3**(11), 1472 (2017).

36. C. V. Thompson, "Solid-State Dewetting of Thin Films," Annu. Rev. Mater. Res. **42**(1), 399–434 (2012).

37. M. Brehm, H. Lichtenberger, T. Fromherz, and G. Springholz, "Ultra-steep side facets in multi-faceted SiGe/Si(001) Stranski-Krastanow islands," Nanoscale Res. Lett. **6**(1), 70 (2011).

38. M. Bollani, D. Chrastina, A. Fedorov, R. Sordan, A. Picco, and E. Bonera, "Ge-rich islands grown on patterned Si substrates by low-energy plasma-enhanced chemical vapour deposition," Nanotechnology **21**(47), 475302 (2010).

39. A. Rätz, A. Ribalta, and A. Voigt, "Surface evolution of elastically stressed films under deposition by a diffuse interface model," J. Comput. Phys. **214**(1), 187–208 (2006).

40. B. Li, J. Lowengrub, A. Rätz, and A. Voigt, "Review article: Geometric evolution laws for thin crystalline films: modeling and numerics," Communications in Computational Physics **6**(3), 433 (2009).

41. M. Salvalaglio, A. Voigt, and S. Wise, "Doubly degenerate diffuse interface models of surface diffusion," Mathematical Methods in Applied Science **44**(7), 5385–5405 (2021).

42. W. Jiang, W. Bao, C. V. Thompson D, and J. Srolovitz, "Phase field approach for simulating solid-state dewetting problems," Acta Mater. **60**(15), 5578–5592 (2012).

43. M. Salvalaglio, R. Backofen, R. Bergamaschini, F. Montalenti, and A. Voigt, "Faceting of Equilibrium and Metastable Nanostructures: A PhaseField Model of Surfsace Diffusion Tackling Realistic Shapes," Cryst. Growth Des. **15**(6), 2787–2794 (2015).

44. M. Salvalaglio, M. Selch, A. Voigt, and S. M. Wise, "Doubly degenerate diffuse interface models of anisotropic surface diffusion," Mathematical Methods in Applied Science **44**(7), 5406–5417 (2021).

45. R. Backofen, S. M. Wise, M. Salvalaglio, and A. Voigt, "Convexity splitting in a phase field model for surface diffusion," Int. J. Num. Anal. Mod. **16**, 192–209 (2019).

46. COMSOL Multiphysics v. 5.6., COMSOL AB Stockholm, Sweden, www.comsol.com.

47. Lumerical 3D Electromagnetic Simulator, https://www.lumerical.com/products/fdtd/.

48. J. Berzins, S. Indrisiunas, K. Van Erve, A. Nagarajan, S. Fasold, M. Steinert, G. Gerini, P. Gecys, T. Pertsch, S. M. Baumer, and F. Setzpfandty, "Direct and High-Throughput Fabrication of Mie-Resonant Metasurfaces via Single-Pulse Laser Interference," ACS Nano **14**(5), 6138–6149 (2020).

49. N. Granchi, M. Montanari, A. Ristori, M. Khoury, M. Bouabdellaoui, C. Barri, L. Fagiani, M. Gurioli, M. Bollani, M. Abbarchi, and F. Intonti, "Near-field hyper-spectral imaging of resonant Mie modes in a dielectric island," APL Photonics **6**(12), 126102 (2021).

50. N. A. Butakov and J. A. Schuller, "Designing Multipolar Resonances in Dielectric Metamaterials," Sci. Rep. **6**(1), 38487 (2016).

51. T. Hinamoto and M. Fujii, "MENP: an open-source MATLAB implementation of multipole expansion for nanophotonics," OSA Continuum **4**(5), 1640–1648 (2021).